



Exploring the Transition Reversal Mechanism in Hypersonic Boundary Layers with Consideration of Leading-Edge Receptivity

Ming Dong¹, Lei Zhao²

Abstract

This work is motivated by the unresolved influence of nose bluntness on hypersonic boundary-layer transition. Linear stability theory explains why small increases in bluntness delay transition, but it cannot account for the reversal of this trend at larger bluntness. This reversal is believed to arise from the growth of non-modal perturbations, yet their receptivity to freestream disturbances has not been quantified. In this paper, we introduce a highly efficient shock-fitting harmonic linearized Navier-Stokes (SF-HLNS) method to quantify non-modal perturbation receptivity. We show that this receptivity mechanism plays the dominant role in the transition-reversal phenomenon. By coupling SF-HLNS with nonlinear parabolized stability equations and secondary-instability analysis, we accurately predict the onset of transition across a range of nose radii. Comparison with experimental data confirms both the reliability and efficiency of our theoretical framework.

Keywords: Hypersonic boundary layer transition, bluntness, receptivity, shock-fitting, harmonic linearized Navier-Stokes

1. Introduction

Laminar-turbulent transition in hypersonic boundary layers is of particular interest due to its relevance to surface drag and heat transfer on high-speed flying vehicles. This task becomes even more challenging when a hypersonic boundary layer features a blunt leading edge, a common design choice for hypersonic vehicles to prevent damage from the extreme heat loads at the stagnation point. Windtunnel experiments [1, 2, 3, 4, 5] have revealed that the effect of nose bluntness on transition location is not monotonic. For configurations with relatively small bluntness, an increase in nose radius leads to a delay in transition; however, the opposite effect occurs when the nose radius surpasses a certain threshold. This phenomenon, known as the transition reversal phenomenon, is influenced by several factors, including the Mach number, Reynolds number, and the level of background noise.

Depending on the instability property of the boundary layer and the environmental perturbation level, the boundary-layer transition proceed along two distinct routes: (1) natural transition, in which modal instabilities (such as the Mack modes) accumulate to finite amplitude; (2) bypass transition, in which the non-modal modes (streaks) reach nonlinear saturation phase and trigger secondary instability with high growth rates. Experimental observations [5] show that at small bluntness the transition onset is dominated by two-dimensional disturbances consistent with planar Mack instability. By contrast, at larger bluntness the transition front develops longitudinal streaks, aligning with a bypass transition driven by non-modal perturbations.

Evidently, increasing the leading-edge bluntness intensifies the entropy layer forming from the nose region. Linear stability theory (LST) shows that this strengthened entropy layer has a stabilizing effect on Mack modes in the downstream boundary layer, explaining the observed delay in transition for small nose radii. However, LST cannot capture the growth of non-modal disturbances, so alternative methods are required. One such approach is the optimal growth theory (OGT), which treats perturbation evolution as an input "Coutput problem and seeks the maximum energy amplification over a specified spatial interval

¹Institute for Mechanics, Chinese Academy of Sciences, dongming@imech.ac.cn

²Department of Mechanics, Tianjin University, leizhao@tju.edu.cn

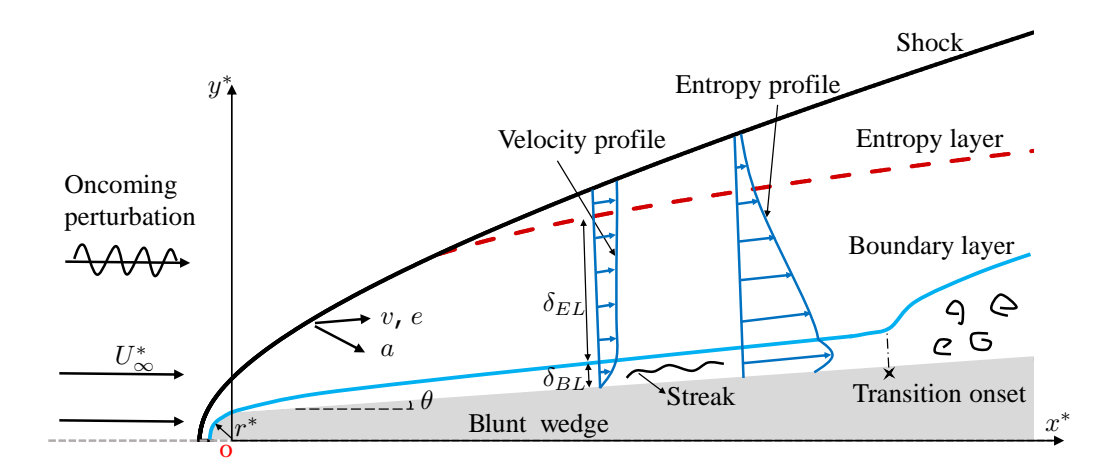


Fig 1. Sketch of the physical model, where a', b' and b' denote acoustic, vortical and entropy disturbances, respectively.

[6, 7]. A major limitation of OGT, however, is its neglect of receptivity of the non-modal perturbations to freestream forcing, which is crucial for describing the transition-reversal phenomenon.

In this paper, we will particularly focus on developing a highly efficient numerical approach, the shock-fitting harmonic linearized Navier-Stokes (SF-HLNS) approach, designed to quantitatively describe the excitation of boundary-layer non-modal perturbations by freestream perturbations. Then, we will show the nonlinear evolution and secondary instability of the non-modal perturbations, and finally predict the transition onset to compare with experimental data.

2. Methodology

2.1. Physical problem

The physical model to be considered is a blunt wedge with a semi-tip-angle θ and a radius r^* embedded in a hypersonic stream with zero angle of attack, as sketched in Figure 1. A detached bow shock wave forms from the leading edge region, and a boundary layer and an entropy layer form in the region sandwiched between the shock and the wall. In the free stream, any small perturbations can be decomposed into a superposition of acoustic, vortical and entropy disturbances. Any of the three components introduced in the oncoming stream can interact with the bow shock and transmit to all the three components behind the shock. These perturbations can further penetrate the entropy and boundary layers, generating either the modal or non-modal perturbations.

In the dimensionless form, the system is described in the Cartesian coordinate system (x,y,z), and the time is denoted by t. the governing equations are the dimensionless compressible Navier-Stokes (N-S) equations. Two key controlling parameters emerge, the Reynolds number Re and the Mach number M.

2.2. Freestream forcing

The freestream disturbance in the uniform stream $\mathbf{u}_{\infty} = (1,0,0)$ can be expressed as

$$\boldsymbol{\varphi}_{\infty}'(x,y,z,t) = \frac{\varepsilon_{\infty}}{2} \hat{\boldsymbol{\varphi}}_{\infty} e^{\mathrm{i}(k_1 x + k_2 y + k_3 z - \omega t)} + c.c., \tag{1}$$

where $\mathbf{k} = (k_1, k_2, k_3)$ and ω are the wave-number vector and the frequency of the disturbance, respectively, ε_{∞} measures the disturbance amplitude, and c.c. denotes the complex conjugate. Denote the

declination angle by

$$\vartheta = \tan^{-1}(k_2/k_3). \tag{2}$$

The acoustic, entropy, and vortical perturbations exhibit distinct dispersion relations, which are outlined as follows.

(i) An acoustic wave could propagate either faster or slower than the base flow, which are referred to as the fast and slow acoustic waves, respectively. The dispersion relations of the two waves can be expressed

$$\omega = k_1 \pm \frac{1}{M} |\boldsymbol{k}|,\tag{3}$$

where the plus and minus signs distinguish the fast and slow acoustic waves, respectively. The eigenfunction, normalized by the amplitude of the pressure fluctuation, reads

$$(\hat{\rho}, \hat{u}, \hat{v}, \hat{w}, \hat{T}, \hat{p})_{\infty} = (M^2, \pm \frac{k_1}{|\mathbf{k}|} M, \pm \frac{k_2}{|\mathbf{k}|} M, \pm \frac{k_3}{|\mathbf{k}|} M, (\gamma - 1) M^2, 1).$$
(4)

(ii) For an entropy wave, we have the dispersion relation

$$\omega = k_1, \tag{5}$$

and the eigenfunction is

$$(\hat{\rho}, \hat{u}, \hat{v}, \hat{w}, \hat{T}, \hat{\rho})_{\infty} = (1, 0, 0, 0, -1, 0)^{T}.$$
(6)

(iii) For a vortical wave, the dispersion relation is the same as (5), but the engenfunction is changed to

$$(\hat{\rho}, \hat{u}, \hat{v}, \hat{w}, \hat{T}, \hat{p})_{\infty} = (0, \hat{u}_{\infty}, \hat{v}_{\infty}, \hat{w}_{\infty}, 0, 0)^{T}, \tag{7}$$

where $k_1\hat{u}_{\infty}+k_2\hat{v}_{\infty}+k_3\hat{w}_{\infty}=0$. For normalization, we let $\sqrt{\hat{u}_{\infty}^2+\hat{v}_{\infty}^2+\hat{w}_{\infty}^2}=1$, but we still need another condition to uniquely determine the values of \hat{u}_{∞} , \hat{v}_{∞} and \hat{w}_{∞} . Introduce the vertical vorticity $\Omega_2 \equiv k_3 \hat{u}_{\infty} - \ k_1 \hat{w}_{\infty}$, then the oncoming perturbation field can be expressed as

$$(\hat{u}_{\infty}, \hat{v}_{\infty}, \hat{w}_{\infty}) = \frac{(-k_1 k_2 + k_3 \tilde{A}, k_1^2 + k_3^2, -k_2 k_3 - k_1 \tilde{A})}{\tilde{B}} \operatorname{sgn}(k_2). \tag{8}$$

where $\tilde{A}=\hat{\Omega}_2|\pmb{k}|{\rm sgn}(k_2)/\sqrt{k_1^2+k_3^2-\hat{\Omega}_2^2}$, $\tilde{B}=(k_1^2+k_3^2)|\pmb{k}|/\sqrt{k_1^2+k_3^2-\hat{\Omega}_2^2}$, and ${\rm sgn}(k_2)=1$ for $k_2\geq 0$ and = -1 for $k_2 < 0$.

2.3. Shock-fitting harmonic linearized Navier-Stokes (SF-HLNS) approach

To study the perturbation evolution, we need to first calculate the base flow solving the steady N-S equations. Then, we calculate the receptivity of the boundary-layer non-modal perturbations to the perturbations in the oncoming stream. The latter can be an acoustic wave, an entropy wave or a vortical wave. After interacting with the bow shock, the three types of perturbations are all excited. Then, these perturbations propagate to the boundary layer through the potential region sandwiched between the shock and the boundary-layer edge, eventually excite boundary-layer non-modal perturbations. To describe this process is challenging, and in this paper, we develop a novel SF-HLNS approach.

The principle idea of the SF-HLNS approach is to perform Fourier transform with respect to t and z for the linearize N-S system, and impose shock-fitting method at the bow shock position to determine the upper boundary condition. A distinct feature of this system is the movement of the shock excited by the unsteady oncoming perturbation. Thus, the perturbation field φ' and the shock-movement H' are expressed in the harmonic form,

$$\boldsymbol{\varphi}'(\xi,\eta,\zeta,\tau) = \frac{\varepsilon}{2} \hat{\boldsymbol{\varphi}}(\xi,\eta) \exp[\mathrm{i}(k_3\zeta - \omega\tau)] + \text{ c.c.}, \tag{9a}$$

$$H'(\xi,\zeta,\tau) = \frac{\varepsilon}{2}\hat{H}(\xi)\exp[\mathrm{i}(k_3\zeta - \omega\tau)] + \text{ c.c..}$$
 (9b)

Case	Mach number M	Oncoming temperature T_{∞}^*	$\begin{array}{c} \text{Wall} \\ \text{temperature} \\ T_w^* \end{array}$	Reynolds number Re	Nose radius r^*	semi-tip-angle θ
Α	5.96	87K	290K	3.34×10^{4}	1 mm	4°
В	5.96	87K	290K	1.67×10^{5}	5 mm	4°
С	5.96	87K	290K	3.34×10^5	10 mm	4°

Table 1. Controlling parameters for receptivity studies.

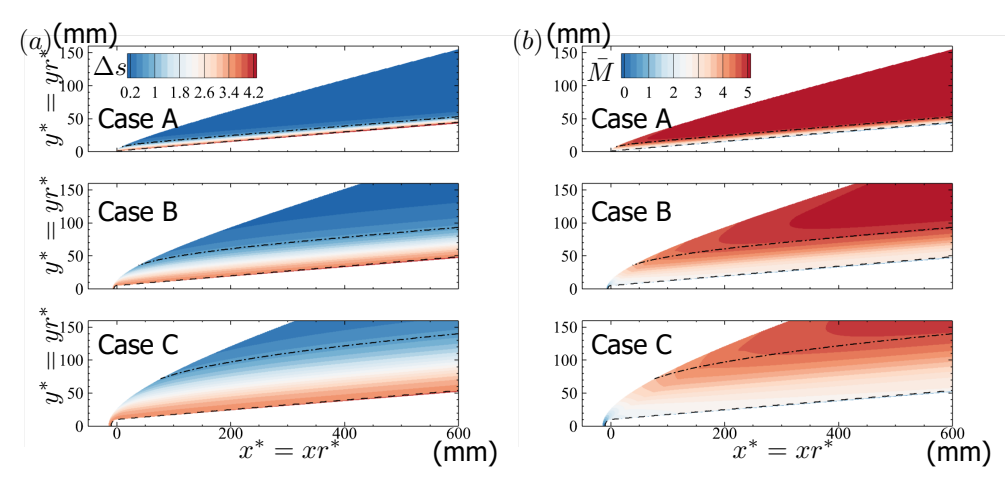


Fig 2. Contours of the entropy increment (a) and local Mach number (b) in the x-y plane for the three cases. The edges of the boundary layer and entropy layer are marked by dashed and dash-dotted lines, respectively.

Substituting (9) into the linearised N-S equations, we derive the SF-HLNS equation system,

$$\mathcal{L}_1\hat{\boldsymbol{\varphi}}(\xi,\eta) + \mathcal{L}_2\hat{H}(\xi) = 0, \tag{10}$$

where \mathcal{L}_1 and \mathcal{L}_2 are the the linear operators. The boundary conditions for system (10) consist of no-slip, isothermal conditions at the wall, as well as the linearized Rankine-Hugoniot relation at the shock, based on the incoming perturbations. Additionally, the compatibility relation is also imposed at the shock. Detailed formulas and algebraic derivations can be found in the work of [8].

3. Numerical results

3.1. Receptivity of non-modal perturbations

Three case studies as outlined in Table 1 are selected. For perturbation evolution, we adopt a two-digit identifier to denote different case studies. The first digit distinguishes the nose radius (Reynolds number) selected from Table 1, while the second digit indicates the freestream perturbation, with 'f', 's', 'e' and 'v' denoting the fast acoustic, slow acoustic, entropy and vorticity waves, respectively. For instance, case Bf signifies a case study involving a nose radius $r^* = 5 \text{mm}$ subject to a fast acoustic forcing.

The contours of the entropy increment and local Mach number for the three cases are compared in Fig. 2, showing a notable expansion of the entropy layer with increasing the nose radius. Performing linear instability analyses, we find that there is no unstable Mack mode in the computational domains

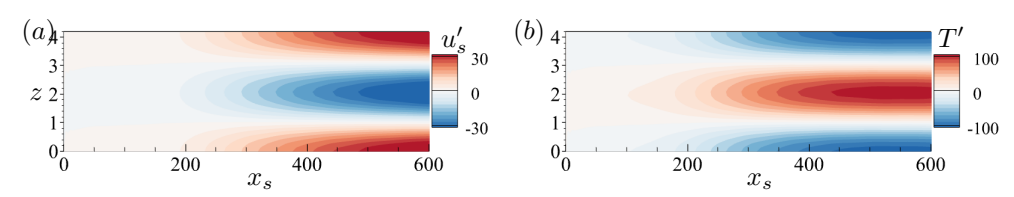


Fig 3. Contours of the streaky structure for case Av with $\omega=0$, $k_3=1.5$ and $\vartheta=15^\circ$ in $z-x_s$ plane at a fixed $y_n=1.2$. (a): u_s' ; (b): T'.

for the three cases, and the unstable entropy-layer modes are found to be growing with rather mild rate, indicating that the transition is unlikely to be triggered by the natural transition route.

As pointed out by [9] and [10], the most amplified non-modal perturbations in boundary-layer flows often exhibit a longitudinal streaky structure attributed to the lift-up mechanism, commonly known as streaks. In figure 3, we present the contours of the velocity and temperature perturbation in the $z-x_s$ plane at $y_n=1.2$ for case Av at $\omega=0$, illustrating prominent streaky structures. The receptivity processes of the non-modal perturbations to each type of freestream forcing, at various frequencies, wavenumbers, inclined angles, are all studied, which help identify the most amplified non-modal perturbations. To ensure a fair comparison of the receptivity efficiency, the energy of freestream perturbations across different case studies needs to be rescaled. Drawing inspiration from [11], we introduce a positive definite energy norm:

$$\mathcal{E}(\hat{\boldsymbol{\varphi}}; x_s, y_n) = ||\hat{\boldsymbol{\varphi}}||_{\mathcal{E}} = \hat{\boldsymbol{\varphi}}^{\mathsf{H}} \boldsymbol{M} \hat{\boldsymbol{\varphi}}, \tag{11}$$

where the superscript H presents the conjugate transpose, and

$$\boldsymbol{M} = \operatorname{diag}\left(\frac{\bar{T}}{\gamma M^2 \bar{\rho}}, \bar{\rho}, \bar{\rho}, \bar{\rho}, \frac{\bar{\rho}}{\gamma (\gamma - 1) M^2 \bar{T}}\right). \tag{12}$$

In the freestream, the energy norm is denoted by $\mathcal{E}_{\infty} \equiv \mathcal{E}(\hat{\varphi}_{\infty})$. Thus, for freestream acoustic, entropy and vortice disturbances illustrated in (2.2), the corresponding energy norms are given by

$$\mathcal{E}^a_{\infty}=2M^2,\quad \mathcal{E}^e_{\infty}=\frac{1}{(\gamma-1)M^2},\quad \mathcal{E}^v_{\infty}=1.$$

At each streamwise location x_s , we define the total energy encompassing the wall-normal perturbation profile as

$$\bar{\mathcal{E}}(\hat{\boldsymbol{\varphi}}; x_s) = \int_0^{y_s} \mathcal{E}(\hat{\boldsymbol{\varphi}}; x_s, y_n) dy_n, \tag{13}$$

where the upper band of the integral is selected as the edge of the entropy layer. Figure 4 compares the streamwise evolution of the normalised total energy $\bar{\mathcal{E}}(x_s)/\mathcal{E}_{\infty}$ across all the cases involving different nose radii and freestream perturbations. The red, green and blue solid lines depict the results for cases Av, Bv and Cv, respectively. It is evident that in the downstream region, the total energy of the non-modal perturbation excited by freestream vortical perturbations decreases as the nose radius r^* expands, with the decrease for relatively larger r^* values being rather mild. Conversely, in cases forced by freestream acoustic and entropy perturbations, depicted by the symboled and dashed lines, the excited perturbations achieve greater downstream energy as the nose radius increases. Upon examining the magnitude of the excited perturbations by unity energy forcing, it is evident that the receptivity of boundary-layer non-modal perturbations in downstream positions to freestream vortical perturbations is rather ineffective, whereas the receptivity to freestream fast or slow acoustic and entropy perturbations is comparable, with the acoustic receptivity demonstrating slightly superior effectiveness. Particularly, the nose-region response to freestream acoustic and entropy forcing is reinforced with increasing nose radius, which could be the dominant factor contributing to the heightened receptivity efficiency observed in the downstream region.

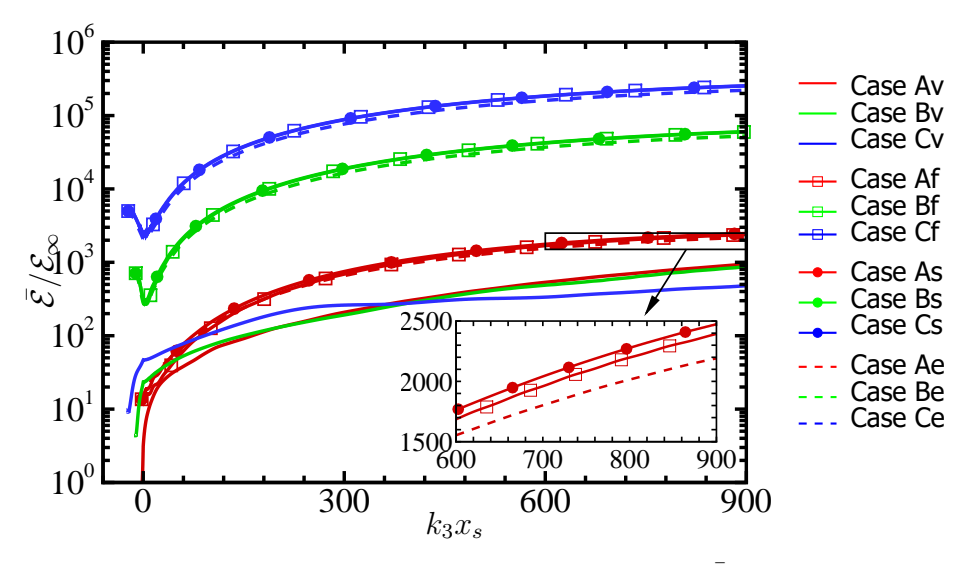


Fig 4. Streamwise evolution of the normalised total energy $\bar{\mathcal{E}}/\mathcal{E}_{\infty}$ across all the cases, where $\omega=0$, $k_3^*=1.5~\mathrm{mm}^{-1}$ and $\vartheta=15^{\circ}$.

Nose	Reynolds	Transition onset	Transition onset
radius	number	location	Reynolds number
r^*	$Re(\times 10^5)$	x_{tr}	$Re_t(\times 10^6)$
1.20 mm	0.696	129	8.98
1.80 mm	1.044	72	7.52
2.00 mm	1.160	43	4.99
2.60 mm	1.508	30	4.52
3.00 mm	1.740	23	4.00
	radius r* 1.20 mm 1.80 mm 2.00 mm	$ \begin{array}{cccc} \text{radius} & \text{number} \\ r^* & Re(\times 10^5) \\ \hline 1.20 \text{ mm} & 0.696 \\ \hline 1.80 \text{ mm} & 1.044 \\ \hline 2.00 \text{ mm} & 1.160 \\ \hline 2.60 \text{ mm} & 1.508 \\ \hline \end{array} $	radius number location r^* $Re(\times 10^5)$ x_{tr} 1.20 mm 0.696 129 1.80 mm 1.044 72 2.00 mm 1.160 43 2.60 mm 1.508 30

Table 2. Parameters for case studies.

Notably, we have also performed OGT to predict the energy growth of the non-modal perturbations for comparison, and a reversed trend, showing a decrease in non-modal energy growth as the nose radius increases, is observed, which directly contradicts the experimental observations.

3.2. Nonlinear evolution of the non-modal perturbations and its secondary instability

To pursue a direct comparison with the experimental data [5], we choose five cases with various nose radii (Reynolds numbers) as outlined in Table 2. Performing nonlinear parabolized stability equation (NPSE) initiated from the small perturbations obtained by SF-HLNS calculations, we can calculate the nonlinear evolution of non-modal perturbations. Fig. 5 demonstrates the base flow for case E. The streaky structures are clearly visible, with their amplitude increasing downstream along x. At a downstream location x=146, pronounced gradients are apparent in both the y_n and z directions, suggesting the potential streak instabilities.

Figure 6 displays the secondary instability properties of the streaky base flow at x=12 for case E. Five unstable branches of the fundamental SI modes are identified, among which mode I is the most unstable. The phase speed of mode I ranges approximately from 0.6 to 0.7, closely resembling that observed in case A. Remarkably, the maximum growth rate for the current profile is almost 0.3, significantly greater than that in cases A to D. This indicates that increasing the nose radius not only enhances the

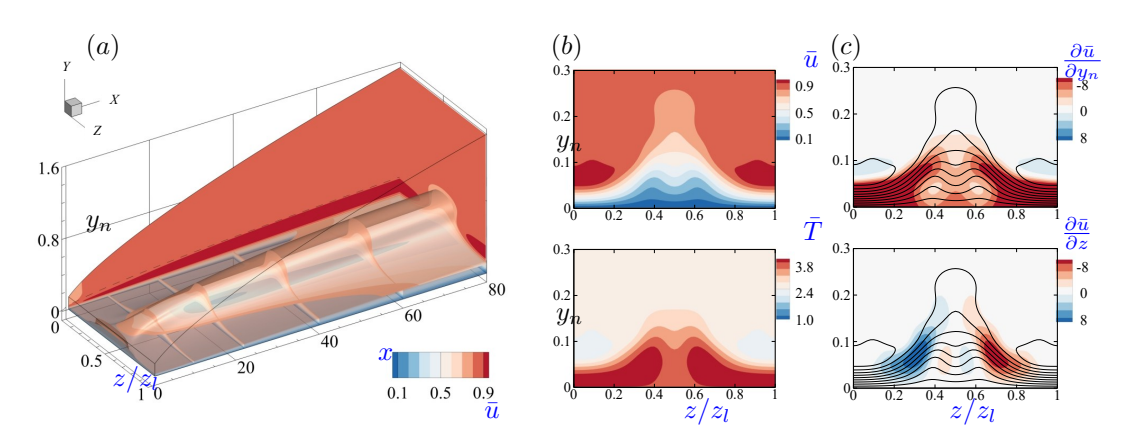


Fig 5. Demonstration of the streaky base flow for case E. (a) Contours of \bar{u} in the entire computational domain; (b) contours of \bar{u} and \bar{T} at x=146; (c) Contours of $\partial \bar{u}/\partial y_n$ and $\partial \bar{u}/\partial z$ at x=146.

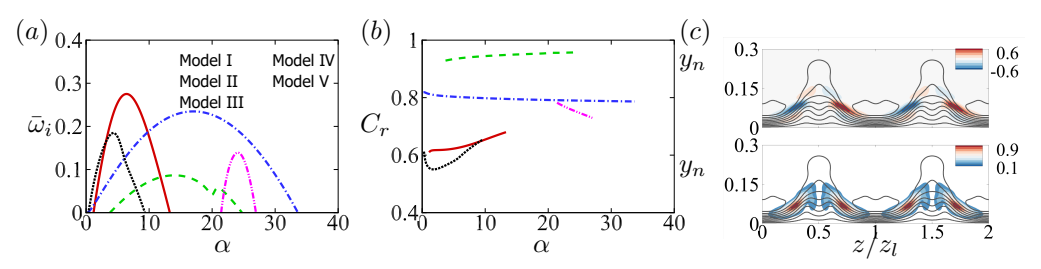


Fig 6. Temporal bi-global analysis of the fundamental SI modes for case E at x=12. (a,b) Dependence on α of $\bar{\omega}_i$ and C_r . (c) The real part (top) and modulus (bottom) of the eigenfunction $\mathrm{e}^{\mathrm{i}\,\sigma_d k_3 z}\,\hat{u}_{SI}(y_n,z)$ of mode I with $\alpha=6.4$, for which $\bar{\omega}_i=0.275$. The eigenfunction is normalised by its maximum.

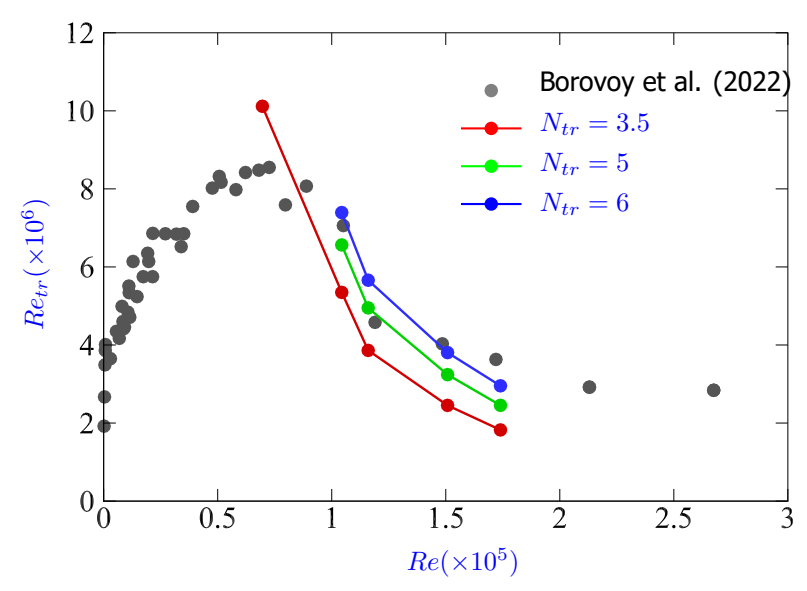


Fig 7. Comparison of the transition Reynolds number Re_{tr} predicted by the e-N approach (solid lines) with the experimental data (black circles). Three values of N_{tr} are selected.

receptivity of the non-modal perturbations but also promotes the amplification of secondary instability modes, consequently leading to an earlier onset of transition.

3.3. Comparison of the theoretical prediction with the experimental data

The amplitude accumulation of the secondary instability modes can be predicted by integrating their growth rates along the streamwise location, which is the principle of the e-N method. Based on this method, we can estimate the bypass transition onset based on a suitable transition threshold N_{tr} . The selection of the threshold N_{tr} is empirical, as prescribing the receptivity of secondary instability modes in streaky base flows is not straightforward. However, as the background noise level in the wind tunnel experiments remains almost unchanged, the receptivity efficiency of the SI modes can be assumed to be comparable across different nose-radius configurations. Therefore, we can reasonably choose a consistent N_{tr} for all the cases considered. Based on this concept, we predict Re_{tr} for three N_{tr} values --3.5, 5 and 6--as shown by the solid curves in figure 7. Notably, all three curves display a consistent trend: an increase in Re leads to a decrease in Re_{tr} , indicating an upstream shift in the transition onset with increased the nose bluntness. Additionally, due to the relatively high growth of the SI modes, the discrepancies among the three curves are not large. The figure also includes experimental results from [5], indicated by circles, which agree overall with our theoretical predictions when Re is above 0.7×10^5 , the critical Reynolds number for the transition reversal phenomenon. At lower Reynolds numbers, the transition is likely triggered by the natural route, dominated by the accumulation of Mack instability, distinct from the mechanism considered in this study. Despite this, the agreement at relatively high Re values confirms that our transition prediction approach not only captures the physical mechanisms of transition for large bluntness observed in experiments, but also provides a quantitative method to describe the bypass transition process stemming from the receptivity of non-modal perturbations.

4. Concluding remarks

Motivated by experimental observations of transition reversal in hypersonic boundary layers, we introduce a highly efficient and accurate shock-fitting harmonic linearized Navier-Stokes (SF-HLNS) approach to systematically quantify the receptivity of non-modal perturbations to freestream acoustic, entropy,

and vortical forcing. Our numerical results reveal that the non-modal perturbations are more susceptible to freestream acoustic and entropy disturbances than to vortical ones, with an optimal spanwise wavelength comparable to the downstream boundary-layer thickness. Crucially, as the nose bluntness increases, receptivity to acoustic and entropy forcing intensifies, reproducing the transition reversal trend seen in experiments at larger bluntness. We also examine the credibility of the optimal growth theory (OGT) on describing the evolution of non-modal perturbations: although OGT captures the general streaky structure downstream, it fails to predict the early-stage evolution and energy amplification accurately.

Based on the SF-HLNS downstream perturbation profiles, we then apply nonlinear parabolized stability equations (NPSE) to follow streak evolution and perform bi-global stability analysis to assess secondary instabilities. By combining computed growth rates with an appropriate transition threshold, we predict the transition onset in excellent agreement with experimental data.

Compared with traditional LST, PSE, and conventional HLNS methods, the present SF-HLNS approach fully accounts for bow shock and entropy layer effects and their interaction with perturbations. Moreover, each SF-HLNS calculation takes under five minutes, three to four orders of magnitude faster than DNS, making it a powerful tool for future studies of hypersonic blunt-body boundary-layer transition under realistic environmental disturbances.

References

- [1] K. Stetson. Shock tunnel investigation of boundary-layer transition at M = 5.5. *AIAA J.*, 5:899--906, 1967.
- [2] K. Stetson. Nosetip bluntness effects on cone frustum boundary layer transition in hypersonic flow. In *16th Fluid and Plasmadynamics Conference*, pages AIAA Paper 1983--1763. AIAA, 1983.
- [3] V. I. Lysenko. Influence of the entropy layer on the stability of a supersonic shock layer and transition of the laminar boundary layer to turbulence. *J. Appl. Mech. Tech. Phys.*, 31:868--873, 1990.
- [4] S. Schneider. Summary of hypersonic boundary-layer transition experiments on blunt bodies with roughness. *J. Spacecr. Rockets*, 45:1090--1105, 2008.
- [5] V. Y Borovoy, V. N Radchenko, S. V Aleksandrov, and V. E Mosharov. Laminar-turbulent transition reversal on a blunted plate with various leading-edge shapes. *AIAA J.*, 60(1):497--507, 2022.
- [6] P. Andersson, M. Berggren, and D. S. Henningson. Optimal disturbances and bypass transition in boundary layers. *Phys. Fluids*, 11(1):134--150, 1999.
- [7] P. Paredes, M. M. Choudhari, and F. Li. Blunt-body paradox and improved application of transient-growth framework. *AIAA J.*, 56(7):2604--2614, 2018.
- [8] L. Zhao and M. Dong. Excitation of non-modal perturbations in hypersonic boundary layers by free stream forcing: shock-fitting harmonic linearised Navier--Stokes approach. J. Fluid Mech., 1013:A44, 2025.
- [9] L. N. Trefethen, A. E. Trefethen, S. C. Reddy, and T. A. Driscoll. Hydrodynamic stability without eigenvalues. *Science*, 261(5121):578--584, 1993.
- [10] P. J. Schmid. Nonmodal stability theory. Annu. Rev. Fluid Mech., 39(1):129--162, 2007.
- [11] L. M. Mack. Boundary-layer stability theory. Jet Propulsion Laboratory, 1969. No. 900--277.